Investigations of Hot-Pressed ^{6}LiInSe$_2$ as a Ceramic Scintillator

By

Joseph Edward Bell

Dissertation

Submitted to the Faculty of the

Graduate School of Vanderbilt University

in partial fulfillment of the requirements

for the degree of

DOCTOR OF PHILOSOPHY

in

Physics

June 30, 2021

Nashville, Tennessee

Approved:

Richard Haglund, Ph.D.

Norman Tolk, Ph.D.

Ashley Stowe, Ph.D.

Arnold Burger, Ph.D.

To my Mother and Father.

ACKNOWLEDGMENTS

TABLE OF CONTENTS

LIST OF TABLES

LIST OF FIGURES

CHAPTER 1

Introduction and Background

1.1   Radiation and Detectors

1.1.1   Radiation

Radiation is the emission of energy from a source in the form of electromagnetic waves or particles and is divided into two categories: nonionizing and ionizing. The low-energy nonionizing radiation, such as radio waves and visible light do not have the required energy to remove electrons from atoms. Nonionizing radiation does have sufficient energy to excite electrons to a higher energy state which results in an increase in temperature. On the contrary, high-energy ionizing radiation such as gamma and x-rays do have sufficient energy to remove electrons from atoms and molecules making long exposure potentially dangerous to living tissue[2]. Neutrons are another form of radiation that can be detrimental to living tissue. These subatomic particles have no net charge which make them difficult to detect. They have the highest penetrating power and can be blocked by concrete or hydrogen-rich materials.

Alpha and beta particles are examples of charged radiation. Alpha particles, also known as helium nuclei are positively charged particles emitted from the nuclei of radioactive elements. They contain two protons and two neutrons. These particles have a short range of only a few centimeters in air and can be stopped with with only a few microns of solid material. A beta particle has a mass equal to 1/1837 that of a proton and is also emitted from the nucleus of a radioactive element during the decay of an unstable atom. A beta particle with a negative charge is an electron while one wuth a positive charge is a positron. Beta particles can be blocked with thin sheets of metal or plastic [3].

Ionization is the process of adding or removing one or more electrons from atoms or molecules thereby creating ions. Ionization can occur at high temperatures in electrical discharges, nuclear radiation or high-intensity lasers [3]. Excitation is the process by which

energy is transferred to a system leaving it at higher energy level. Excitation occurs once the incident particle deposits its energy into the active volume of the detector. The particle will form free electron-hole pairs along its path of travel. An electon-hole pair forms when an electron is excited from the valance band to the conduction band. The electron is now free until it loses its energy. A hole is region in the lattice that was vacated by an excited electron. For charged particles, it is relatively easy to adjust the electronic settings connected to the detector to see all of the alpha or beta particles. When this happens, the detector is said to have a counting efficiency of 100% [2]. There are more steps involved in detecting uncharged such as neutrons.

1.1.2 Neutron Interactions

Charged radiation continuously interacts with any electron present due to their positive or negative charge. Uncharged radiation lacks this trait making them difficult to detect. Gamma rays, and neutrons, two examples of uncharged radiation go through a significant number of interactions within the active volume of a detector before being counted. These interactions cause the particle to lose some or all of its energy. If these interactions do not occur within the detector, the uncharged particle can exit the detector without being counted. This uncertainty in detecting uncharged particles is why there needs to be an exact figure for the detector efficiency.

Some neutrons may pass through a detector with no interaction at all, while others may change energies and velocities. Some neutrons may be absorbed. Each of these events has a unique probability of happening. The probability of a neutron interacting with the target media depends on the concept of a cross-section. A neutron cross-section expresses the probability of interaction between the incident neutron and target nucleus. It also allows the calculation of the reaction rate and is measured in barns. A barn is roughly the cross-sectional area of a uranium nucleus and is equal to $10^{-28} m^2$.

The neutron cross-section can be used to classify isotopes. Isotopes that absorb neu-

trons and either decay or keep the neutron are know as neutron absorbers. This reaction will have a neutron capture cross-section. If the isotope undergoes fission, it will have a fission cross-section. The nuclear interaction will scatter the neutron which gives them a neutron scatter cross-section. The probability of interaction is expressed using the total cross-section. The total cross-section is the sum of the absorption and scattering cross-section and is seen in equation (1.1) below.

$$\sigma_T = \sigma_S + \sigma_A \tag{1.1}$$

Here, σ_T is the total cross-section, σ_S is the scattering cross-section and σ_A is the absorption cross-section. Elements with a large scatter cross-section and low mass are known as neutron moderators. Moderators reduce the speed of fast neutrons with minimal absorption leaving them as thermal neutrons.

1.1.3 Detectors

Because neutrons have no intrinsic charge, they must be detected indirectly. A common way of detecting neutrons is through the neutron activation process. This process involves the capture of free neutrons by atomic nuclei which causes the nuclei to become heavier and enter an excited state. The excited nucleus immediately undergoes fission, releasing measurable products. Regardless of what type of radiation is being measured, the efficiency of the device needs to be determined. This efficiency is used to relate the number of pulses counted to the number of photons incident on the detector. There are two classes of efficiency: absolute and intrinsic. Absolute efficiency, ε_{abs} is shown in equation (1.2) below:

$$\varepsilon_{abs} = \frac{P_{rec}}{Q_s} \tag{1.2}$$

where P_{rec} is the number of recorded pulses and Q_s is the number of radiation quanta

emitted by the source. Absolute efficiency is dependent on a number of elements with the properties of the detector and the distance to the source being the main contributors.

Detector intrinsic efficiency no longer includes the solid angle as a factor and depends on the material of the detector, the radiation energy, and the thickness of the detector. The intrinsic efficiency, ε_{int} is shown in equation (1.3) below:

$$\varepsilon_{int} = \frac{P_{rec}}{Q_d} \tag{1.3}$$

where P_{rec} is the number of recorded pulses and Q_d is the number of radiation quanta incident on the detector. There is still a dependence on the distance from the source to the detector because the path length of the radiation changes with spacing.

Total and peak efficiencies further describe the response of a detector. Total efficiency is the probability that the radioactive source will produce a pulse regardless of size. Peak efficiency is the probability that the radioactive source will release all of its energy within the detector. For practical use, there is a finite threshold set in the detector to distinguish between background pulses and actual radiation from a source. For a complete characterization of a detectors efficiency, the total and peak efficiency need to be considered. Once the efficiency for the detector is known, the absolute activity of a radioactive source can be measured.

Using the definition of intrinsic peak efficiency, one can find the number of radiation quanta emitted by a source. It is given by equation (1.4) below.

$$S = N\frac{4\pi}{\varepsilon_{ip}\Omega} \tag{1.4}$$

In this equation S is the number of radiation quanta emitted by the source, N is the number of recorded events, ε_{ip} is the detectors intrinsic peak efficiency and Ω is the solid angle subtended by the detector at the source position. This equation can be rewritten to find the

intrinsic peak efficiency,ε_{ip}, as shown below in equation (1.5).

$$\varepsilon_{ip} = N\frac{4\pi}{S\Omega} \tag{1.5}$$

A solid angle is defined by the surface area of a sphere subtended by the lines and by the radius of that sphere. It is a dimensionless unit that defines how large an object appears from one point [4]. The solid angle ,Ω, is an integral over the detectors surface facing the source as shown in equation (1.6) below.

$$\Omega = \int_A \frac{cos\alpha}{r^2} dA \tag{1.6}$$

In this equation, r is the distance between the source and the surface element dA and α is the angle between the surface element and the source direction. If the volume of the source is non-negligible, a second integration over the entire volume of the elements of the source must be calculated. As an example, consider a point source located along the axis of a right cylindrical detector. The solid angle used in this case is given by equation (1.7).

$$\Omega = 2\pi \left(1 - \frac{d}{\sqrt{d^2 + a^2}} \right) \tag{1.7}$$

In this equation Ω is the solid angle, d is the distance from the source, and a is the radius of the detector.

Dead time is an important factor when discussing detectors because there exists a minimum amount of time that must separate two events so they can be recorded as single pulses. Radioactive decay is random which implies there is chance that events will become lost because they occur too quickly after a preceding event. These losses become severe when there is a high-count rate. Corrections for dead time must be calculated to get a more accurate reading. There are two models of dead time behavior: paralyzable and nonparalyzable.

In paralyzable dead time, each subsequent event extends the dead time which leads

to prolonged periods of no pulse detection. In a nonparalyzable detector, any event that happens within the dead time is lost and has no effect on the behavior of the detector. To make corrections, it is ideal to have prior information of the dead time. Most often, this is not the case because dead time can vary depending on operating conditions. Dead time will have to be calculated directly in these situations[2].

A common method used to determine dead time is called the two-source method. This method observes the counts of two sources individually and in combination. Due to non-linearity of counting losses, the observed rate of the combined sources will be less than the sum of the two sources counted separately. Let m_1 be the observed rate of source 1, m_2 be the observed rate of source 2 and m_{12} be the combined rate of both sources. Let mb be the measured background and τ be the dead time. Dead time is calculated in equation (1.8).

$$\tau = \frac{x(1 - \sqrt{1 - z})}{y} \tag{1.8}$$

such that

$$x \equiv m_1 m_2 - m_b m_{12} \tag{1.9}$$

$$y \equiv m_1 m_2 (m_{12} + m_b) - m_b m_{12} (m_1 + m_2) \tag{1.10}$$

$$z \equiv \frac{y(m_1 + m_2 - m_{12} m_b)}{x^2} \tag{1.11}$$

1.2 Scintillation

1.2.1 Introduction

A scintillation detector is an instrument used to detect ionizing radiation with the use of a crystalline or polycrystalline scintillating material. Through the scintillation process, the material interacts with incident radiation and produces light. The photons emitted are within or near the visible spectrum. The scintillation device detects this light and, with the appropriate equipment, outputs a signal. The device contains a scintillator that generates

photons from incident radiation. In this work, ^{6}LiInSe$_2$ is the scintillator of choice. It also contains a photodetector such as a photomultiplier tube (PMT), a charge coupled device (CCD) or a photodiode. The PMT is the instrument that converts photons to photoelectrons via the photoelectric effect.

Fluorescence is the phenomenon that underlays scintillating materials. It is the fast emission of light with a delay on the order of 10 ns from the time of energy deposition to the interaction between radiation and the material. In first approximation, light output follows an exponential decay with the evolving number of photons described, $N_{photons}(t)$, in equation (1.12).

$$N_{photons}(t) = \frac{N_{tot}}{\tau_d} e^{-t/\tau_d} \tag{1.12}$$

where N_{tot} is the total number of emitted photons, τ_d is the characteristic decay constant. Time evolution of light output does not solely operate as a single exponential decay and is better seen as a two component system with one slow and one fast element. This is seen in equation (1.13) below.

$$N_{photons}(t) = Ae^{-t/\tau_A} + Be^{-t/\tau_B} \tag{1.13}$$

where A and B are normalisation constants and τ_A and τ_B are decay constants of the fast and slow components.

Light yield is one of the defining characteristics of a scintillator. Light yield is the measure of a materials response to incident radiation and is defined by the ratio between the total number of emitted photons detected by the PMT to the deposited energy in the scintillator. In order for a scintillator to be efficient, it must have certain properties. Most importantly, it should convert the kinetic energy of the particles into detectable light with a high quantum efficiency. This is defined in the equation (1.14) below.

$$Q = \frac{N_{pe}}{N_{ph}} \tag{1.14}$$

Here, the quantum efficiency, **Q**, is equal to the number of photoelectrons, N_{pe}, divided

7

by the total incident photons, N_{ph}. The conversion should be linear meaning that the light yield is proportional to the deposited energy over a wide range. The medium should be transparent to its wavelengths to increase light capture efficiency. The decay time should be short enough such that fast signal pulses can be generated. The emission of light should be a detectable frequency. No material meets all these criteria at the same time so there is always a compromise when choosing the material [2][5].

1.2.2 Scintillation Process

Scintillators such as ^{6}LiInSe$_2$ used in this work produce luminescence from incident radiation. Photon emission is typically aided by the addition of a dopant as an activator site. The scintillation mechanism in concerns the electronic band structure of the material. Electrons are excited to the conduction band with a dopant adding energy levels in the band gap. Activators/dopants are limited by the number of vacancies in the crystal lattice. If the dopant levels are too high, the semiconductor becomes degenerate meaning it behaves more like a metal than a semiconductor. This is known as the Moss-Burstein effect where the bandgap energy is increased so that the electron carrier concentration exceeds the conduction band density of states [6]. Fortunately, ^{6}LiInSe$_2$ doesn't need an activator to detect radiation making it a very useful material. Phosphorescence may occur due to electrons being trapped in energy levels that forbid de-excitation [5].

The scintillation process is one of the oldest methods for detection and spectroscopy and begins with incident radiation on a scintillator [2] and can be seen in the figure 1.1 below. When ionizing radiation enters the scintillator, atoms are excited along the path of radiation. If this deposited energy can overcome the band gap energy electrons from the valence band will migrate to the conduction band. This excitation creates electron-hole pairs. Electrons are negatively charged atomic particles while the electron hole is the lack of an electron where one could exist in an atomic lattice. electon-hole pairs are fundamental in the carrier and recombination processes.
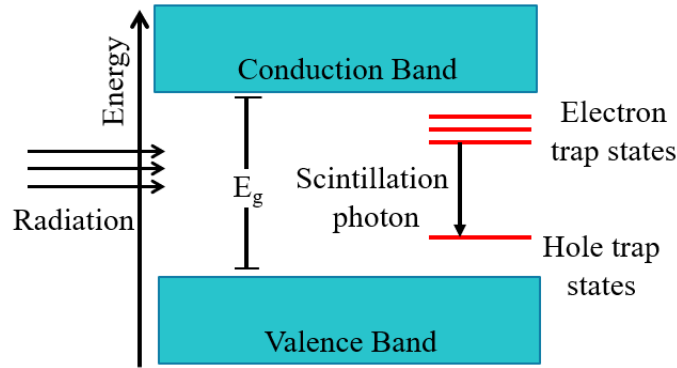
Figure 1.1: Energy band structure showing excitation and photon emission of an activated crystalline scintillator.

In undoped scintillators and semiconductors, Fermi levels exist in the band gap between the valence and conduction bands. The band gap is an energy range where no electronic states can exist. It is the energy difference between the two bands and is the minimum required energy to excite electrons to the conduction bad. The valance band is below the Fermi level and when unexcited, is completely occupied. On the contrary the conduction band is above the Fermi level and completely empty. Once the required energy is deposited in the material and excitation happens, electrons and holes will flow freely in the conduction band and valence band respectively. Carrier generation is the process described above where electrons gain energy producing two charge carriers.

Recombination is the process where an electron loses energy and reoccupies the energy state of the electron hole. Generation and recombination are always occurring both optically and thermally. When a material is at thermal equilibrium, generation and recombination are balanced such that the net charge carrier density stays constant. The concentration of electrons in the conduction band, n_i, is given equation (1.15) below.

$$n_i = AT^{3/2}e^{-E_g/2kT} \tag{1.15}$$

where A is a proportionality constant, E_g is the band gap energy at temperature 0 kelvin, k is Boltzsmann's constant and T is the temperature of the semiconductor. Under the effects

of an applied electric field, electrons and holes will drift with an average velocity:

$$v_e = \mu_e(E,T) \times E \tag{1.16}$$

$$v_h = \mu_h(E,T) \times E \tag{1.17}$$

where μ_e and μ_h are mobility functions of electrons and holes repsectively, E is the electric field and T is the temperature. The occupation of energy states is governed by Fermi-Dirac statistics which describe the distribution of particles over energy states in systems.

In high qualtiy scintillators, radiative recombination is dominant meaning that upon de-excitation, a photon is released. A photomultiplier tube (PMT) is a type of vacuum tube used to detect light in the ultraviolet, visible and near-infrared wavelengths on the electromagnetic spectrum. Photomultiplier tubes are useful in light detection of very weak signals because they multiply the incident light to usable ranges. Once a scintillation crystal is adhered to the window of the PMT, the scintillation events can be counted. Incoming radiation will interact with the crystal via the scintillation process and produce photons. Some of the photons will interact with the photocathode which converts these photons into photoelectrons by the photoelectric effect. These photoelectrons are accelerated and focused onto the first dynode by the focusing electrode. The multiplication occurs when photoelectrons encounter the dynodes. This contact will release additional electrons that accelerate towards the next dynode in the chain. At the end of the dynode chain is an anode that collects the multiplied secondary electrons and outputs them to proper characterization equipment [7][2].

1.3 Crystal Growth

Crystal growth is a major part in the development of new materials that require a vast range of electrical and optical properties. The devices created from crystal growth — semiconductors and scintillators — can be either single crystal or polycrystalline. A single crystal is a solid material that is composed of atoms in a repeating three-dimensional pattern —

a crystal lattice— that is formed by the type of bonds within the crystal. A polycrystalline material on the other hand is characterized by a multitude of small crystals separated by boundaries.

Growth of single crystals is essentially a transformation into the solid state from either a solid, liquid or vapor state. From an initially disordered state, there are three steps to crystal formation: achievement of supersaturation/supercooling, nucleation, and growth of nuclei into single crystals of distinct phases. Supersaturation is a metastable state in a chemical solution where the solute exceeds the concentration specified by value equilibrium solubility. Supercooling is the process of lowering the temperature of a liquid or gas below its freezing point without it solidifying. The driving force of crystal growth begins with supersaturation of supercooling and therefore need to be maintained to achieve high quality crystals [8].

Nucleation is the close packing of a few molecules to form a small crystal embryo. This may occur spontaneously or artificially induced and is heavily influenced by fluctuations in Gibbs free energy. When the surface area to volume ratio of the embryo is large, there is an increase in Gibbs free energy. As more molecules incorporate themselves into the crystal embryo making it stable, the Gibbs free energy becomes less than that of the melt. This causes spontaneous molecular growth. Nucleation from melt is governed by Gibbs-Thompson relation seen in (1.18)below.

$$\Delta H_m \left(\frac{T_m - T_r}{T_m} \right) = \frac{2\sigma V}{r} \tag{1.18}$$

Here, T_r is the melting point of a crystal embryo with radius r and T_m is the melting point of a large crystal. The two types of nucleation are heterogenous and homogenous. Heterogenous nucleation occurs at the surface and is more common than homogenous nucleation. Heterogenous nucleation occurs at the phase boundaries such as the solid-liquid interface in Bridgman growth. At these sites, the surface energy is lower which reduces the free energy barrier [9].

Crystallization can be described in terms of nucleation and growth with Gibbs free energy being integral in both aspects. Current understanding of crystal growth began with Gibbs phase equilibrium concept. Commonly referred to as the phase rule, this principle governs systems in thermodynamic equilibrium where their states can be described by pressure, volume, and temperature. Gibbs free energy is used to calculate the maximum reversible work that may be performed in a system at constant temperature and pressure. This energy is minimized when a system reaches chemical equilibrium. The formula for Gibbs free energy, G, and its corresponding implicit differentiation are shown in equation (1.19) below:

$$G = H - TS, \Delta G = \Delta H - T\Delta S \tag{1.19}$$

In this definition, H is defined as enthalpy, T is defined as temperature and S is defined as entropy. The ΔG term represents change in energy, ΔH is change in enthalpy and $T\Delta S$ is change in entropy [8].

1.3.1 Defects during Growth

Primary and secondary are the two types of inclusions found during crystal growth and are distinguished according to their origin. Primary inclusions occur during growth and are known as key defects because they are the source of other defects. These inclusions propagate with the growth front and cause the formation of stress centers. Primary inclusions are caused from foreign particles, solvent inclusions if grown from a solution, and solute precipitations from impure or doped melts. Secondary inclusions are solute impurities that arise after growth in the solid state during slow cooling or annealing. These solutes are caused by the supersaturation of solutes below the growth temperature.

Foreign particulates in the melt can lead to multiple nucleation sites. This is typically not an issue because the crystallization's disjoining pressure repulses the foreign particulates away from the growth front [10]. This force can be overcome depending on the chemical and physical nature of the particulates and growth conditions. If the inclusions do

not segregate to the opposite face of the growth front, the common practice is to filter until the inclusions can be removed.

The distribution of dopants is an important parameter for crystals grown from melts. If the effective distribution coefficient is less than one, a high dopant concentration will be in front of the growth interface. On the contrary, for higher growth rates the solute concentration can become supersaturated meaning the dopant will be incorporated into the crystal as growth continues. Therefore, dopant precipitation is parameterized by the effective distribution coefficient, the timescale of solute diffusion, and growth rate [8].

The effective distribution coefficient k_{eff} is the ratio of the distribution of impurities between the ambient phase and the crystal and is shown in equation (1.20):

$$k_{eff} = \frac{k_0}{k_0 + (1 - k_0)exp(-R\delta/D)} \tag{1.20}$$

where k_0 is the equilibrium distribution coefficient R is the growth rate, D is the diffusion constant and δ is the thickness of the diffusion boundary layer. When $k_{eff} < 1$ impurities accumulate as growth continues forming an area of high concentration in the diffusion boundary layer surrounding the crystal. This changes the chemistry at the diffusion boundary layer which ultimately effects growth rate, diffusion rates and the formation of a gradient boundaries and point defects parallel to the growth surface. The changes can happen even if the crystal is grown under constant conditions.

1.3.2 Device Performance

Depending on the concentration, defects from impurities can have negative effects on the performance of the device. Defects can influence the structural properties of a device by creating vacancies and interstitials that change the lattice constant and grains that affect single crystallinity. They can also effect the chemical properties of the detector because they play a role in chemical reactions. Their redistribution also creates inhomogeneities in the crystals composition. The electronic properties are influenced because defects can

occupy a specific state in the band structure. Scattering properties are changed because defects interact with phonons, photons, electrons and many other particles.

All thermodynamic processes attempt to minimize free energy. In the crystallization process, if the atoms and molecules are perfectly packed in a three-dimensional ordered structure, the free thermodynamic potential of Gibbs energy is minimal. This means that the atomic bonds are saturated regularly. The sum of these atomic bonds is the potential H while the enthalpy of the crystals internal energy is equation (1.21) below.

$$U = H - PV \qquad (1.21)$$

where U is the internal energy P is pressure and V. Because of this, the process of ordering crystal periodicity is governed by the minimization of enthalpy. This also means that there is an impossible minimal entropy S that gains significance as temperature T increases. This is governed by the basic equation of the thermodynamic potential of Gibbs free energy seen in equation (1.22) below.

$$G = U + PV - TS = H(\downarrow) - TS(\uparrow) \rightarrow min \qquad (1.22)$$

In this equation, the up and down arrows correspond to increasing and decreasing respectively as the Gibbs energy approaches a minimum. Therefore, crystallization is governed by two opposite process: regular and defective arrangement of atoms and molecules. Knowing this, it is impossible to grow a perfect crystal because at thermodynamic equilibrium, crystal perfection is limited by the concentration of native point defects. Disregarding changes in volume, defect type, and assuming constant pressure, the equilibrium defect concentration n can be found from the changes in thermodynamic potential as seen equation (1.23) below

$$\Delta G = \Delta H_d - \Delta S_d T \rightarrow min \qquad (1.23)$$

where ΔG is the change in Gibbs free energy $H_d = nE_d$ representing the change in internal energy due to n defects, and S_d being the change of entropy. In the equation (1.23) above

$$S_d = k_b \ln \frac{N!}{n!(N-n)!} \tag{1.24}$$

where k_b is Boltzmann constant and N is the total number of possible sites. The total defect formation energy is dependent on many temperature dependent factors which can only be calculated experimentally from high purity crystals and extremely sensitive analytical techniques.

Point defects exist in all devices above absolute zero because they increase configurational entropy leading to a decrease in free energy. These point defects control the basic properties of a crystal and are sometimes purposefully introduced to alter the overall performance of the device. In optical devices such as the crystals and ceramics used in this work, the density and distribution of point defects will alter the transmittance, refractive index and birefringence of the device [8].

1.3.3 Bridgman Growth

The crystals in this study were grown using a modified Bridgman method in a vertical setup. This method, named after Percy Williams Bridgman, is a method used for growing single crystals. In general, a crystal is formed from a slow solidification from melted material. The process involves lowering molten material into a region that is below the melting point. This can be at room temperature or into a different temperature region of the furnace. An illustration of Bridgman growth is seen in figure 1.2 below.

For the crystals grown in this project, a furnace with two temperature zones was used. This was to ensure reproducibility. To grow large single crystals, certain criteria must be met. First, the lowering speed must be less than the speed of crystallization and slow enough so the latent heat from solidification can be depleted through conduction. Secondly, there should be a nucleation point at the bottom of the aperture that holds the material.
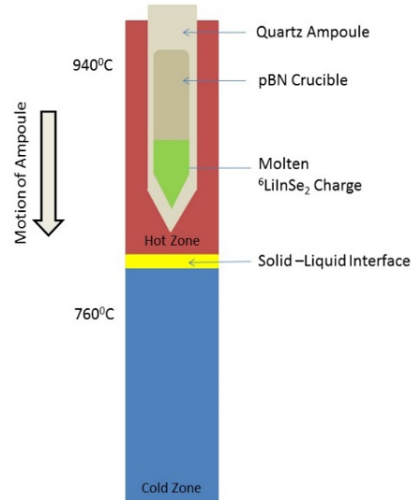
Figure 1.2: Illustration of vertical Bridgman growth method.

There are orientations within the crystal that are more favorable for growth. Regardless of the starting orientation, the most energetically favorable orientation will eventually become the main growth structure.

To increase the amount of usable crystal, it is encouraged to have a nucleation point that starts with the more favorable orientation. This allows the crystal to grow based off the nucleation point's orientation [11][8]. There are advantages in using this growth method. First, there is direct control of the thermal gradient. This allows for precise temperature control at various locations in the melt. Secondly, buoyancy forces allow for the separation of multiple secondary phases. Lastly, because this is a closed system, the risk of contamination is greatly reduced.

1.4 Photon Interactions in Solids

1.4.1 Introduction

Light will interact with matter many ways and is classified by various parameters. One can classify the plethora of optical properties into three categories: reflection, propagation, and transmission. When light enters a material, some of the light is reflected off the front surface while the rest enters the material. If any of the transmitted light reaches the back

surface, it can be reflected once more or transmitted through the medium. Therefore, the amount of transmitted light is related to the reflectivity of the front and back surfaces and also the propagation of light through the material[12][13].

1.4.2 Interactions

Refraction which causes light waves to lose velocity leads to the bending of light rays as described by Snell's law below in equation (1.25).

$$n_1 sin\theta_1 = n_2 sin\theta_2 \tag{1.25}$$

Here, n_1 is the incident index n_2 is the refracted index, θ_1 is the incident angle and θ_2 is the refracted angle [13]. Absorption can occur during the propagation of light through a medium if the frequency of incident light is in resonance with the transition frequencies of the atoms in the medium. If this criterion is met, the photon will be attenuated along its path in the medium. When light enters a transparent material, a portion of its energy is dissipated as heat which results in a decrease in intensity. The unabsorbed light is transmitted through the medium and is seen as a certain color.

Luminescence is defined as the spontaneous emission of light by excited atoms in a solid-state material [12]. Absorption is one of the ways atoms enter an excited state and can be accompanied by luminescence as the light propagates through the medium. Luminescence is not always possible due to the time it takes for light to be re-emitted. If this is the case, the excited atoms will dissipate the excitation energy as heat before the radiative emission occurs.

Scattering plays a major role in the propagation of light through a medium. Scattering is when light changes direction in a medium and potentially changes its frequency. This phenomenon does not decrease the number of photons, but it does limit the amount of photons traveling in the forward direction. Because of this, scattering has the same attenuative effect as absorption. If the energy of the photon is unchanged, the scattering is elastic. Sim-

ilarly, if the energy is changed the scattering is inelastic. Scattering is caused by changes in the refractive index typically caused by impurities, defects, or inhomogeneities. This attenuated light decreases exponentially as it propagates according to equation (1.26).

$$I(z) = I_0 exp(-N\sigma_s z) \tag{1.26}$$

where $I(z)$ is the intensity at position z, I_0 is the optical intensity at $z = 0$, N is the number of scattering centers per unit volume and σ_s is the scattering cross-section. There are many types of scattering that affect the attenuation of light. Rayleigh scattering is when the size of the scattering center is much smaller than the wavelength of light. The size of a scattering particle is governed by the ratio in equation (1.27),

$$x = \frac{2\pi r}{\lambda} \tag{1.27}$$

where r is the particles radius and λ is the wavelength of light. The scattering cross-section varies with the wavelength of light and is characterized by equation (1.28)

$$\sigma_s(\lambda) \approx .\frac{1}{\lambda^4} \tag{1.28}$$

For Rayleigh scattering events in inhomogeneous materials, shorter wavelengths are scattered more strongly than longer wavelengths. The inelastic scattering of a photon by a free charged particle is called Compton scattering. An event where the photon decreases in energy is known as a Compton effect while an increase in photon energy is called inverse Compton scattering. The relationship between the shift in wavelength and scattering angle is determined by the equation (1.29):

$$\lambda' - \lambda = \frac{h}{mc}(1 - cos\theta) \tag{1.29}$$

where λ is the initial wavelength, λ' is the wavelength after scattering, h is Planck's constant, m is electron mass, c is the speed of light and θ is the scattering angle. The elastic scattering of charged particles by Coulomb interactions is known as Rutherford scattering. This type of scattering is best seen in the classical experiment by Hans Geiger and Ernest Marsden in 1909 where they fired a beam of alpha particles against gold nuclei. Neither the alpha particles nor gold nuclei were internally excited yet some of the particles were deflected by very large angles. Rutherford characterized the number of patciles per unite area incident to the detector, $N(\theta)$, by the following equation:

$$N(\theta) = \frac{(N_i n L Z^2 k^2 e^4)}{(4 r^2 K E^2 sin^4(\theta/2))} \tag{1.30}$$

where N_i is the number of incident alpha particles, n is atoms per unit volume in target, L is thickness of target, Z is the atomic number of the target e is electron charge k is Couloumbs constant, r is target-to-detector distance KE is kinetic energy of alpha and θ is the scattering angle.

Photon diffusion is a case where photons traverse a material but rather than being absorbed, they are repeatedly scattered [13]. The interactions in this low absorption and high scattering medium are modeled by the diffusion equation for the photon energy density:

$$\nabla^2 U - \frac{1}{\sigma} \overrightarrow{\nabla} \sigma = 0 \tag{1.31}$$

where σ is opacity, U is photon fluence and ∇ is the del operator. The propagation of radiation through a medium is affected by the radiative transfer mechanisms in absorption, emission, and scattering processes and can be described by the equation of radiative transfer. This equation states that as a beam of radiation travels through a material, it will lose energy by absorption, gain energy by emission, and redistribute energy by scattering. The

differential form is seen below:

$$\frac{1}{c}\frac{\partial}{\partial t}I_v + \hat{\Omega}\cdot\nabla I_v + (k_{v,s}+k_{v,a})I_v = j_v + \frac{1}{4\pi}k_{v,s}\int_\Omega I_v d\Omega \tag{1.32}$$

where I_v is the enrgy flowing across an area element, c is the speed of light, j_v is the emission coefficent $k_{v,s}$ is the scattering opacity, $k_{v,a}$ is the absorption coefficient and the $\frac{1}{4\pi}k_{v,s}\int_\Omega I_v d\Omega$ term controls the radiation scattered from other directions onto a surface.

Photons behave differently in isotropic and anisotropic materials and therefore have different parameters. Assuming the material is isotropic, the diffusion equation is typically written as

$$\frac{\partial\phi(r,t)}{\partial t} = \nabla\cdot[D(\phi,r)\nabla\phi(r,t)] \tag{1.33}$$

where $\phi(r,t)$ is the density ϕ of the diffusing material at position r and time t and $D(\phi,r)$ is the diffusion coefficient for density ϕ at position r. When the diffusion coefficient depends on the the density, diffusion is linear. Diffusion in anisoptropic materials must be modeled three dimensionally as seen below:

$$\frac{\partial\phi(r,t)}{\partial t} = \sum_{i=1}^{3}\sum_{j=1}^{3}\frac{\partial}{\partial x_i}\left[D_{ij}(\phi,r)\frac{\partial\phi(r,t)}{\partial x_j}\right] \tag{1.34}$$

If the diffusion coefficient is constant, the anisotropic diffusion equation reduces to equation (1.35) below which models how particles diffuses through a material.

$$\frac{\partial\phi(r,t)}{\partial t} = D\nabla^2\phi(r,t) \tag{1.35}$$

The diffusion equations above are derived from Fick's law of diffusion. Fick's first law relates the movement of particles to the gradient of the concentration. Essentially, a solute will move from an area of high concentration to an area of low concentration across

a concentration gradient [12]. In one dimension, this is typically written as:

$$J = -D\frac{d\psi}{dx} \qquad (1.36)$$

where J is the diffusion flux, D is the diffusion coefficient ψ is the concentration and x is position. Two or more dimensions require a gradient operator changing the diffusion flux to the following equation.

$$J = -D\nabla_\psi \qquad (1.37)$$

1.4.3 Index of Refraction

Reflection at the surface is described by the coefficient of reflectivity, R, and while the coefficient of transmission, T, describes the ratio of transmitted power to incident power. If a material neither absorbs nor scatters then by the conservation of energy, the sum of reflectivity and transmission will be equal to one as shown below in equation (1.38)

$$R + T = 1 \qquad (1.38)$$

Light is characterized by its frequency and velocity and is defined by the following equation.

$$E = hv = \frac{hc}{\lambda} \qquad (1.39)$$

Here, E is energy, h is Planck's constant, v is frequency, c is the velocity of light and λ is wavelength. The velocity of light in vacuum is 2.99793 x 10^{10}cm/sec. When light propagates through a medium, its phase velocity will decrease. The decrease in velocity is determined by the ratio between the velocity of light and the phase velocity. This ratio is known as the refractive index as shown in equation (1.40) below.

$$n = \frac{c}{v} \qquad (1.40)$$

The refractive index, n, of a material is equal the ratio of the speed of light in a vacuum, c, and the phase velocity of light through the medium, v. The phase velocity of a material depends on the density. Generally, phase velocity decreases with increasing density. Refractive indexes are different for each wavelength of light which causes dispersion. The refractive index increases with frequency from the infrared to ultraviolet and originates mainly from interband absorption in the UV region. Normal dispersion occurs when the refractive index increases with frequency while anomalous dispersion occurs when it decreases. An example of dispersion is seen when white light is shown through a prism. Blue light is refracted more because of its high index of refraction and therefore has a larger angle of deviation. Furthermore, different frequencies of light require different amounts of time to traverse a medium. A pulse of light with duration t_p must contain a spread of frequencies, Δv, as approximated by the following:

$$\Delta v \approx \frac{1}{t_p} \tag{1.41}$$

Therefore, dispersion causes light pulses to broaden in time as pulses traverse mediums. Pulse spreading is parameterized by group velocity dispersion and is proportional to the second derivative of the refractive index with respect to vacuum wavelength. This is defined by the material dispersion parameter, D below:

$$D = -\frac{\lambda}{c}\frac{d^2 n}{d\lambda^2} \tag{1.42}$$

where λ is wavelength, n is the refractive index and c is the speed of light. The spreading or temporal broadening $\Delta\tau$ of a pulse is given by:

$$\Delta\tau(ps) = |D|\Delta\lambda L \tag{1.43}$$

where $\Delta\tau$ is the spectral width of the pulse and L is the length of the medium. The

Lorentz model describes the behavior of pulses within the normal dispersion region. In the dispersion equation shown in equation (1.42), $d^2n/d\lambda^2$ is negative for frequencies above an absorption line and positive above it. This indicates that because of the vibrational absorption in the infrared, there is a positive material dispersion parameter and a negative one in the visible because of interband absorption in the ultraviolet [12].

1.4.4 Harmonic Oscillator

Bound electrons are assumed to be in a stable orbit about a nucleus with springs acting as restoring forces for small displacements from equilibrium. The Coulomb forces between the electrons and nucleus create an electric dipole with a magnitude proportional to their separation. The natural resonant frequency ω_0 is found using the reduced mass and magnitude of the restoring force. The reduced mass is given by the following equation:

$$\frac{1}{\mu} = \frac{1}{m_e} + \frac{1}{m_N} \tag{1.44}$$

where m_e is the mass of the electron and m_N mass of the nucleus. The mass of the nucleus is much greater than the mass of an electron so $\mu \approx m_e$ is a safe assumption. The natural resonant frequency ω_0 is calculated using the equation (1.45) below:

$$\omega_0 = \sqrt{\frac{K_s}{\mu}} \tag{1.45}$$

where K_s is the spring constant. An electric dipole moment measures polarity and consists of a positive charge $+q$ at position r_+ and a negative charge $-q$ at r_-. The electric dipole moment is defined by the equation:

$$p = q(r_+ - r_-) \tag{1.46}$$

which show that the positive nucleus and negative electron form a dipole moment with magnitude:

$$e|r_N - r_e| \tag{1.47}$$

The nucleus remains stationary while the electrons oscillate backwards and forwards with frequency ω_0. The electric field exerts a force ω on the dipole and if $\omega = \omega_0$, the atom can absorb energy. The absorption coefficient α models the strength of absorption while Beer's law models its exponential decay.

The absorption coefficient, α quantifies the absorption of light in an optical medium and is defined by the fraction of power absorbed per unit length. If a photon is propagating in the z direction with intensity at position z being $I(z)$, the decrease in intensity per unit length dz can be described by:

$$dI = \alpha dz \times I(z) \tag{1.48}$$

which can be integrated to obtain Beers law:

$$I(z) = I_0 e^{-\alpha z} \tag{1.49}$$

where I_0 is the optical intensity at position $z = 0$. The displacement of atomic dipoles in the interactions between a light wave and an atom with a single resonant frequency ω_0 due to bound electrons can be modeled as a damped harmonic oscillator. The electric field of the light wave stimulates oscillations of the atomic dipoles through the forces acting on the electrons. This causes the electron to be displaced which is governed by the following equation of motion:

$$m_e \frac{d^2x}{dt^2} + m_e \gamma \frac{dx}{dt} + m_e \omega_0^2 x = -e\varepsilon \tag{1.50}$$

where m_e is the mass of the electron γ is the damping rate, e is the magnitude of the electric field of the electron and ε is the electric field of the light wave. In a material that contains a significant amount of free electrons, such as semiconductors, there is no restoring force

when they are displaced. This implies the spring constant $K_s = 0$ [12].

1.4.5 Anisotropy

Materials can be segregated based on how the velocity of light changes in the material. Materials that do not depend on the direction of light are called isotropic. An isotropic polycrystalline material displays the same optical properties in all directions meaning photons behave the same in all directions. This means that at each grain boundary, the refractive index is the same which reduces scattering. On the contrary, in anisotropic materials light propagation is dependent on direction of light. This means that at each grain boundary, photons will change direction.

In an anisotropic material, when light travels from one interface to another, it will reflect and refract. The angle of reflected light is equal to the angle of incidence while the angle of refraction is dependent on both the angle of incidence and the refractive index of the other interface. If any of the transmitted light reaches the back surface, it can be reflected once more or transmitted through the medium. One of the common traits of an optically anisotropic material is birefringence. This a property where the refractive index depends on the polarization and direction of light propagation. Birefringence can cause double refraction which is the splitting of light into two distinct light rays which take different paths. These rays are known as ordinary and extraordinary and are orthogonally polarized to each other with the extraordinary ray not following Snell's law.

By generalizing the relationship between polarization P and applied electric field E, one can describe the properties of birefringence by the tensor equation below:

$$P = \varepsilon_0 \chi E \qquad (1.51)$$

where χ is the susceptibility tensor. In this relation, it is assumed that the electric field is applied along an arbitrary direction. In matrix notation, by choosing Cartesian coordinates

x, y, and z to correspond to the principal axes of the crystal χ is seen as the following:

$$\chi = \begin{pmatrix} \chi_{11} & 0 & 0 \\ 0 & \chi_{22} & 0 \\ 0 & 0 & \chi_{33} \end{pmatrix} \tag{1.52}$$

Crystal symmetry is a determining factor in for the components. In cubic crystals, the x, y, and z axes are equivalent and therefore behave isotopically. Being isotropic, these crystals do not have the issue of birefringence. Uniaxial crystals have a single optic axis meaning there is a single direction that governs anisotropy. Rotating around this axis does not change the optical performance of the crystal. Biaxial crystals such as ^{6}LiInSe_2 used in this work contain two optic axes meaning there exist three refractive indices. Because of this, no rotation about an axis will preserve the crystals optical properties. Although there is no symmetry within biaxial crystals, the two optical axes serve as directions in which light may propagate without birefringence [12][13].

CHAPTER 2

Properties of ^{6}LiInSe$_2$

Due to the shortage of ^{3}He, alternative solid state neutron detecting devices have become increasingly common [14][15]. These materials respond to incident radiation by producing photons through scintillation mechanisms or an electrical current in a semiconductor mode [16]. Typically, high resolution single crystal scintillators such as Bi$_4$Ge$_3$O$_{12}$ (BGO) and ^{6}LiInSe$_2$ provide sufficient light yield and decay times to prove useful for real-world applications. Although single crystal scintillators are useful, they can be costly and time intensive to fabricate. To circumvent these issues and many others, research groups have begun investigating ceramic radiation detectors [17] [18][19] [20].

Certain elements are used for neutron detection such as ^{10}B and ^{157}Gd but this work utilizes ^{6}Li [2]. More specifically, ^{6}LiInSe$_2$ is the material of choice for this paper. This material benefits from having ^{6}Li incorporated directly into its structure which makes a dopant unnecessary for neutron detection. Although ^{6}LiInSe$_2$ will be used as a scintillator in this work, it also has the capability of operating in a semiconductor mode [21]. Natural lithium is comprised of two stable isotopes, ^{6}Li and ^{7}Li, with the latter accounting for 92.5% [22]. Compared to natural lithium's neutron capture cross-section of 70.5 barns and ^{7}Li's cross-section of 0.045 barns, ^{6}Li has a very high capture cross-section of 940 barns [23].

The capture cross-section determines the probability of a neutron capture event by ^{6}Li. The reaction for the detection of neutrons is the (n,α) within ^{7}Li. This is defined by the equation (2.1) below.

$$_3^6Li \ + \ _0^1n \ \rightarrow \ _1^3H \ + \ _2^4He \ \ Q-Value: 4.78 MeV \tag{2.1}$$
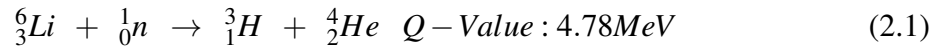
The ^{6}Li increases in energy when the neutron is absorbed causing it to enter an excited state. This quasi-bound compound nucleus stays together until there is sufficient energy concentrated in one neutron to escape the nucleus. This occurs on a time scale of about 10^{-19} seconds. The reaction results in the production of an alpha particle with a charge of +2 and a triton. With a half-life of 10^{-13}s, ^{6}Li* quickly returns to its ground state after the emission of a 0.48 MeV gamma ray. The gamma ray escapes and does not contribute to the detector response [2].

^{6}LiInSe$_2$ crystallizes in the orthorhombic structure and transitions to the chalcopyrite structure after annealing at a pressure of 4.2 GPa. The fundamental and direct absorption edges of ^{6}LiInSe$_2$ are reported to be 2.03 eV and 2.9 eV, respectively [24][25]. The light yield has been reported to be 9,000 photons/MeV with peak emission at 512 nm and decay time constants at 31 ± 1 ns and 143 ± 9 ns [26].

2.1 Ceramics

2.1.1 Introduction

A polycrystalline material is defined by its many small crystallites in various orientations separated by grain boundaries. These small crystallites, also referred to as grains, can be oriented randomly or directed through a growth process. Grain size and orientation play a significant part in light propagation and ultimately the light yield of the detector. There are some conventional ways that light can be scattered which are shown in figure 2.1 below. Light scatter leads to a longer path inside the sample before it exits. This increases the likelihood that the photons will be absorbed by impurities within the ceramic.

Scattering in polycrystalline ceramics can be minimized if the grain size is small and oriented in the same direction. Grinding the material to a fine powder increases the likelihood of this happening. Grain size on the order of tens of nanometers have been shown to produce detectors with effective optical quality in CaF^2 [27]. To manipulate the optical properties of a polycrystalline material, there must be a way to control grain growth.
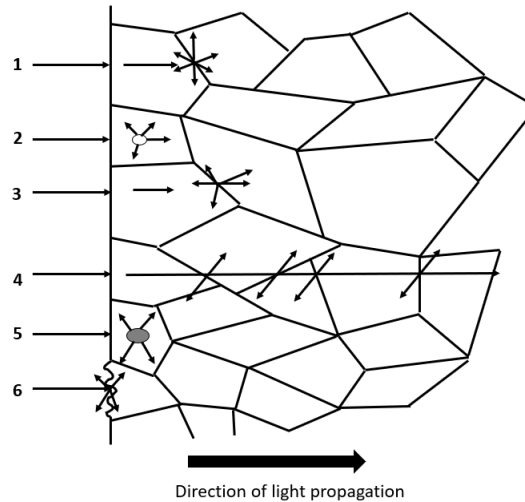
Direction of light propagation

Figure 2.1: The image shows the structure of conventional transparent ceramics, with light scattering and the attenuation of input power through the ceramic. (1) grain boundary, (2) residual pores, (3) secondary phase, (4) double refraction, (5) inclusions and (6) surface roughness [1].

To obtain a uniform grain size after the sample has been pressed, the sintering temperature and time must be optimized. Typically, the material is heated to 2/3 of its melting point. This temperature allows for substantial atomic mobility and can serve as a reference for future sintering experiments. Sintering is the process of compacting and forming a solid mass using heat or pressure without liquefying the material and is an integral part in grain control. Grain growth is typically unavoidable in sintering so various techniques are used to control this phenomenon including adding a dopant, and controlling the influence of Zener pinning by adding a solute.

The addition of solutes is widely used in nanocrystalline materials because they typically segregate at grain boundaries. The accompanying drag force of solute mobility at grain boundaries decreases the rate of grain growth. This phenomenon is known as Zener pinning which deals with the dispersion of particles on the movement of low and high angle grain boundaries in polycrystalline materials. Dopants have a twofold effect because it influences kinetics at the boundary and thermodynamics.

The purpose of sintering is to decrease the surface area which in turn decreases the

excess free energy. This excess of free energy causes particles to become unstable leading to an overall unusable material. Whenever diffusion allows, surface elimination between two or more particles will occur. When this happens, new surface area is created but it is smaller than the previous surface area. During the sintering process, the different interface energies will lead to rotation or rearrangement of grains to decrease the total free energy. This will ultimately produce a uniform ceramic that has minimal light loss [28].

2.1.2 Grain Growth

Grain growth is the size increase of crystallites in a material at high temperatures. The excess energy stored in grains is the driving force behind grain growth. According to Gibbs adsorption theorem, which relates components in contact with a surface to changes in surface tension and energy, grain boundary energy should decrease with the segregation of solutes. From this, one can infer that grain boundary segregation reduces the driving force of grain growth and once low enough, grain growth will stop. The kinetics of grain growth can be described by the following velocity v equation below:

$$v = M_{gb} \left(\frac{\lambda_{gb}}{r} \right)$$ (2.2)

where M_{gb} is the grain boundary mobility, λ_{gb} is grain boundary energy and r is the grain size. By integrating this equation, one can obtain more information as seen below:

$$r^n - r_0^n = kt$$ (2.3)

where r_0 is the initial grain size, t is the annealing time, and k which is a temperature dependent constant that contains the diffusion parameter. In equation (2.3) n is typically greater than or equal to two. Therefore, k can be rewritten as:

$$k = k_0 exp \left(\frac{-Q}{RT} \right)$$ (2.4)

where Q is the activation energy for boundary mobility, R is the molar gas constant, and T is the absolute temperature [28].

2.1.3 Solutes

During grain growth, grain boundary migration will be affected not only by other boundaries but also other imperfections in the material such as vacancies, dislocations and impurities. As mentioned earlier, solutes slow the rate of grain growth. During grain boundary migration, solutes segregate to boundaries and attempt to stay there meaning grain boundaries can only move as fast as their solutes. Dopants and solutes are used to increase this drag force.

Solutes are segregated in various ways during grain growth which lead to a multitude of different drag forces and kinetic models for grain growth. Utilizing the parameters described by Burke, [29] assuming the drag force is independent of the average grain size and there exist a maximum grain size to account for the effects from second phases, impurities, and sample thickness. Once growth velocity stops drag force, f can be represented as the following:

$$f = \frac{M_{gb}\lambda_{gb}}{r_{max}} \tag{2.5}$$

where M_{gb} is the grain boundary mobility, λ_{gb} is grain boundary energy and r_{max} is the maximum grain size. If second phases and inclusions exists but their volume fraction and size distribution are fixed, Burkes assumption that drag force is independent of grain size holds.

The drag force becomes dependent on grain size when the solute excess varies with grain boundary migration. If the drag force from the solute atoms is proportional to the difference between solute concentrations in grain boundaries and the bulk material, then from Michels [30] the drag force can be written as:

$$f = \frac{rM_{gb}\lambda_{gb}}{r_{max}^2} \tag{2.6}$$

Further work from Rabkin [31] showed that drag force should be a function of grain size and velocity as seen below:

$$f = \beta M_{gb} r \frac{dr}{dt} \qquad (2.7)$$

with β being a constant dependent on interface energy and starting radius. Using the classical parabolic equation:

$$\frac{dr}{dt} = \frac{M_{gb} \lambda_{gb}}{r} - f(r) \qquad (2.8)$$

it is seen that grain size is proportional to interface energy and mobility but slowed down by the drag force. From this equation, three models fro grain growth can be derived according to Burke, Michels, and Rabkin:

$$\frac{\alpha}{r_{max}^2} t = \frac{r_0 - r}{r_{max}} + \ln \left(\frac{r_{max} - r_0}{r_{max} - r} \right) \qquad (2.9)$$

$$r = \left[r_{max}^2 - (r_{max}^2 - r_0^2) \exp \left(\frac{-2\alpha t}{r_{max}^2} \right) \right]^{1/2} \qquad (2.10)$$

$$\alpha t = \frac{1}{2}(r^2 - r_0^2) + \frac{1}{3}\beta M_{gb}(r^3 - r_0^3) \qquad (2.11)$$

The difficulties of predicting grain growth do not end with these models because they assume constant grain boundary energy. If the composition of the grain boundary undergoes a change significant enough to disturb the drag force, the grain boundary energy will be affected [8].

CHAPTER 3

Material Preparation

3.1 Synthesis and Growth of Crystals

The creation of the ^{6}LiInSe$_2$ crystals consists of two steps: synthesis and growth. The elements used are lithium-6(5N), indium (5N), and selenium (6N). In the synthesis portion, the ^{6}LiIn alloy and ^{6}LiInSe$_2$ charge are created. In an argon filled glove box, stoichiometric amounts of lithium and indium are placed in a quartz ampoule. Due to the highly reactive nature of lithium, the materials must be placed inside a pyrolytic boron nitride (pBN) crucible before being place in the ampoule to prevent reactions with the quartz. A valve is then fitted to the open end of the ampoule and vacuumed down to 0.5 atm. A hydrogen/oxygen torch is used to seal the quartz ampoule. The sealed ampoule is then loaded into a muffled furnace at a 450° angle with rotation at 7 rpm. The temperature will heat to 750 °C at a rate of 0.7 °C/min. and cool down to room temperature at a rate of 0.7 °C/min.

The second part of the synthesis process is the creation of the ^{6}LiInSe$_2$ charge by vapor transport. Again, the materials are prepared within the argon filled glove box. After weighing the ^{6}LiIn alloy and placing it back inside a pBN crucible, the proper amount of selenium is calculated and placed at the bottom of a quartz ampoule. A quartz stilt is placed on top of the selenium and the pBN crucible on top of that. The ampoule is then sealed at 0.5 atm with a hydrogen/oxygen torch. The ampoule is once again loaded into the muffled furnace at a 45° angle. The furnace will heat to 940 °C at a rate of 0.1 °C/min and cool down to room temperature at 0.1 °C/min. The charge is then returned to the glove box where it is extracted, weighed, and placed into a growth pBN crucible. The crucible is placed in a quartz ampoule and sealed at 0.5atm.

The method used for growth is vertical Bridgman. This consists of having two temperature zones in a furnace. A 24 zone furnace is used for growth with the top zones set to 940 °C and bottom zones set to 760 °C. The ampoule with ^{6}LiInSe$_2$ charge is loaded into

the furnace. It will soak in the hot zone for 16 hours to allow the charge to be completely melted. After the soak, the nucleation point is formed by lowering the ampoule into the solid-liquid interface. The temperature gradient of the interface allows for the most energetically favorable orientation to become dominant . After 4 hours, the nucleation point has formed. The ampoule will then lower at a rate of 7 mm/day until the entire length of the material translates to the cooler region. The translation to the cooler region makes the crystal solidify. The furnace is slowly cooled to avoid potential cracks. After the furnace has cooled to room temperature, the crystal is ready to be removed and examined.

3.2 Ceramic Preparation

The source for all the ceramics made in this body of work come from a ^{6}LiInSe$_2$ crystal made via Bridgman growth. The properties of this crystal were measured. These techniques include, its melting point, absorption edge and most importantly its scintillation properties. This insured that any polycrystalline sample made would be capable of detecting radiation. While in an argon filled glove box, crystalline samples were ground to a fine powder using a mortar and pestle and sifted to sizes ranging from 75 μm to 20 μm. This powder was transferred to stainless steel dies and prepared for pressing. This setup can be seen in figure 3.1 below.
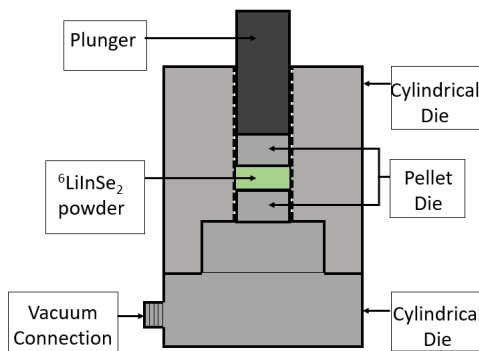

Figure 3.1: Powder form of ^{6}LiInSe$_2$ inside stainless steel die

In lab atmosphere, 5 metric tons were applied to the material for 24 hours at 300 °C. The finished ceramic wafers were removed and sintered at 400 °C for four hours under a

flow of argon gas. After cool-down, samples were sintered again at 450 °C for 1 hour under

vacuum.

CHAPTER 4

Properties of Ceramic ^{6}LiInSe$_2$

4.1   Introduction

The development of ceramic radiation detectors has been ongoing for a number of years. In 1966, Carnall *et al.* showed that a hot pressed polycrystalline CaF$_2$:Dy is virtually identical to its single crystal counterpart when measuring transmittance, refractive index and optical homogeneity [32]. During the late 80's and 90's, researchers showed interest in gadolinium based ceramic scintillators in the forms of (Y,Gd)$_2$ O$_3$: Eu,Pr, and Gd$_2$O$_2$S: Pr, Ce, F with Ce: Gd$_3$Al$_2$Ga$_3$O$_{12}$ eventually making an appearance [19] [20]. Despite the inherent disordered regions of grain boundaries, there are reports of ceramics outperforming their crystal counterparts in terms of brightness and decay time [19] and even afterglow and thermoluminescence [33].

This work will utilize a ceramic version of ^{6}LiInSe$_2$. Similar to Carnall *et al.* [32], the ^{6}LiInSe$_2$ ceramic used in this work is formed from a crystalline version of ^{6}LiInSe$_2$ that had its scintillation properties measured. Using a crystalline version ensured that the ceramic was made from a material proven to be a viable scintillator. Furthermore, in the early stages of crystal growth, the crystal quality was not sufficient enough for practical applications. Instead of resynthesizing ^{6}LiInSe$_2$ powder, unusable pieces of the crystal were crushed into powder.

The choice between using a ^{6}LiInSe$_2$ ceramic or a crystal depends on the application. Generally, when materials are in ceramic form they are faster and less costly to produce. However, these benefits come with a sacrifice. Unlike a single crystal, polycrystalline ceramics contain grains and grain boundaries which scatter light and ultimately lead to a lower light yield and decreased energy resolution. Typically, light can be scattered at grain boundaries, residual pores, inclusions and at the surface roughness of the sample [1]. This

scattering of light correlates to a lower signal via absorption. Increased scattering leads to a longer path inside the sample before it exits. This increases the likelihood that the photons will be absorbed within the ceramic [34].

The information presented will show that the ceramic is a viable option for a radiation detector. In particular, this study shows that a ceramic wafer can be formed using a mechanical press equipped with a heating attachment. Finally, this work will show that a ceramic ^{6}LiInSe$_2$ wafer performs similarly to a single crystal when operated as a scintillator.

4.2   Experimental

4.2.1   Sample Preparation

Similar to Carnall *et al.* [32], the material for all the ceramic wafers in this study were sourced from a ^{6}LiInSe$_2$ crystal. It was synthesized using a two-step method, described in Tupitsyn *et al.* [35] and grown using the Bridgman method, in a vertical setup similar to the method used by Wiggins[26] and Magesh[36]. This process involves lowering molten material into a region that is cooler than the melting point. The slow transition from the hotter region to the cooler region is where crystallization occurs. In this study, a 24 zone Mellen furnace was set to have the top zones at 940°C and the lower zones at 760°C. The molten material lowered at a rate of 7 mm/day to form the crystal. Ceramic sample preparation does not account for the time it takes to create a crystal due to the variability in crystal growth time and because a noncrystalline ^{6}LiInSe$_2$ can be used as the starting material.

While in an argon filled glove box, samples were ground to a fine powder using a mortar and pestle and sifted to sizes ranging from 75 μm to 20 μm. This powder was transferred to stainless steel dies and prepared for pressing. In lab atmosphere, 5 metric tons were applied to the material for 24 hours at 300°C. The finished ceramic wafers were removed and sintered at 400°C for four hours under a flow of argon gas. After cool-down, samples were sintered again at 450°C for 1 hour under vacuum. The porosity of the samples were

determined using the steps provided in [37]. Using the formula in equation (4.10, the porosity for the sample used in this study is 6.4%

$$Porosity\% = \frac{SaturatedMass - DryMass}{ExteriorVolume} \times 100$$

(4.1)

4.2.2 Characterization

A Cary 5000 UV-VIS-NIR spectrophotometer collected the optical absorption data at room temperature. A baseline was set and data was collected from 800 nm to 300 nm. Emission data was collected at room temperature using a Horiba Fluoromax spectrofluo-rometer. Excitation wavelengths of 365 nm and 200 nm were used with entrance and exit slits at 5 nm. Step size was set to 0.5 nm with an integration time of 0.1s. The samples are placed vertically at a $60°$ angle from the incoming excitation beam to ensure sufficient light reached the detector. To evaluate chemical composition, a JEOL scanning electron microscope (SEM) with energy dispersive X-ray spectroscopy (EDS) was performed on the $^6LiInSe_2$ ceramic. Additional chemical composition measurements were conducted with a Thermo Fisher Scientific X-ray photoelectron spectrometer (XPS) microprobe with an attached dual beam ion source for depth analysis.

Scintillation measurements were conducted at room temperature in a dark box using a Hamamatsu R6231-100 PMT coupled to a preamplifier. Connected to the preamplifier via BNC connections are the shaping amplifier, analog-digital converter (ADC) and multi-channel analyzer (MCA). To obtain the absolute light yield, both alpha and neutron sources were directly irradiated to the PMT window and serve as the background. The samples were covered in a layer of Teflon tape with a 1 mm hole for alpha radiation. An ^{241}Am source

was used for alpha radiation tests with an acquisition time of 300 s. A neutron response was obtained using a ^{252}Cf source with an acquisition time of 1800 s. Both the crystal and ceramic use 1000 V bias and a shaping time of 2 μs. From the incident alpha particles, pulse decay times were determined using a two phase exponential association equation. This was done by connecting the output of the PMT directly into an oscilloscope.

4.3 Results and Discussion

4.3.1 Sample

Figure 1 represents a ^{6}LiInSe$_2$ ceramic and crystal on 1 mm transparency. The sizes of the ceramic and single crystal are 0.33 mm x 13 mm diameter and 0.33 mm x 18 mm diameter, respectively. The ceramic sample is visually opaque but has a similar color to the single crystal.
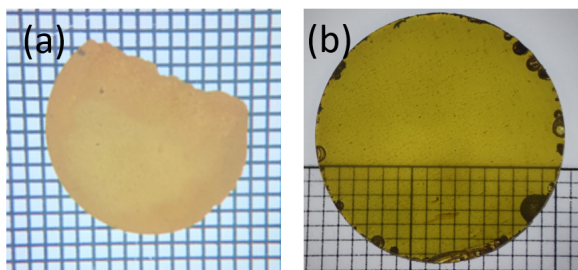

Figure 4.1: Figure 4.1 represents a ^{6}LiInSe$_2$ ceramic (a) and single crystal (b) back-lit wafers on a 1 mm transparency grid. Ceramic and single crystal are 0.33 mm x 13 mm diameter and 0.33 mm x 18 mm diameter, respectively.

4.3.2 Optical absorption

The ceramic sample closely resembles the stoichiometric color of the ^{6}LiInSe$_2$. A UV-Vis spectrophotometer was used to determine light transmission. Results in figure 2 show the ceramic sample is less transparent than its crystal counterpart but still transmits light until around 1.86 eV (667 nm). The absorption edge is shifted significantly in the ceramic which indicates that the ceramic starts absorbing at a much lower energy. The fundamental

and direct absorption edges of $^6LiInSe_2$ are reported to be 2.03 eV and 2.9 eV, respectively [24].
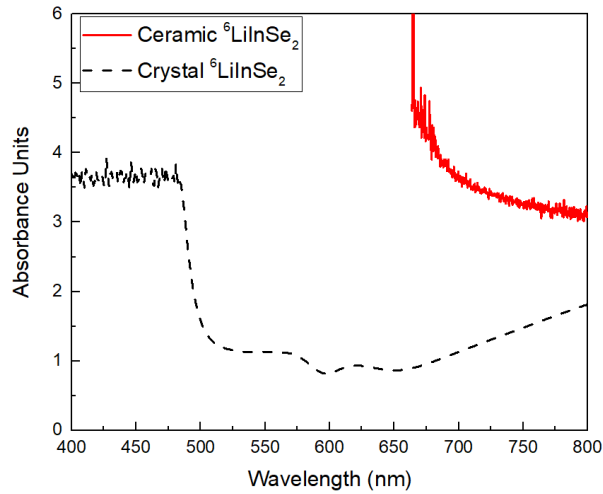

Figure 4.2: Absorption spectra of $^6LiInSe_2$ crystal and ceramic.

The ceramic does not transmit any measurable light through most of the UV-Vis range but at wavelengths above 650 nm, there is about a 2% transmission. Scintillation occurs around 512 nm (2.42 eV) so the position of the absorption edge in the ceramic cannot be seen [26]. The absorption of these photons further implies that there are impurities in the ceramic samples. This can also be seen in the drastic change of color in the ceramic. Scanning electron microscopy with energy dispersive X-ray spectroscopy (SEM/EDS) determines the chemical composition and finds any impurities. As expected, oxygen is present in the ceramic sample which aids in the low energy absorption edge.

4.3.3 Emission

Figure 3 shows the emission data of the ceramic and crystal $^6LiInSe_2$. The samples are placed vertically at a $60°$ angle from the incoming excitation beam. The crystalline sample used an excitation wavelength of 200 nm and produced an emission wavelength at 512 nm which is supported by the claims provided by Wiggins *et al.*[26]. A smaller peak is also seen at 823 nm. In ceramic samples, no emission peaks were seen when using a

200 nm excitation wavelength. A 365 nm excitation wavelength proved to be sufficient and produced an emission peak at 823 nm. Although the ceramic has a significant shift from its crystal counterpart's reported 512 nm emission peak, its emission peak was expected to be above 667 nm due to its absorption edge at 1.86 eV. The 823 nm peak seen in both the ceramic and crystal means that there is a near IR trap state. This trap state is the main source of emission in the ceramic but only a minor source of emission in the crystal.
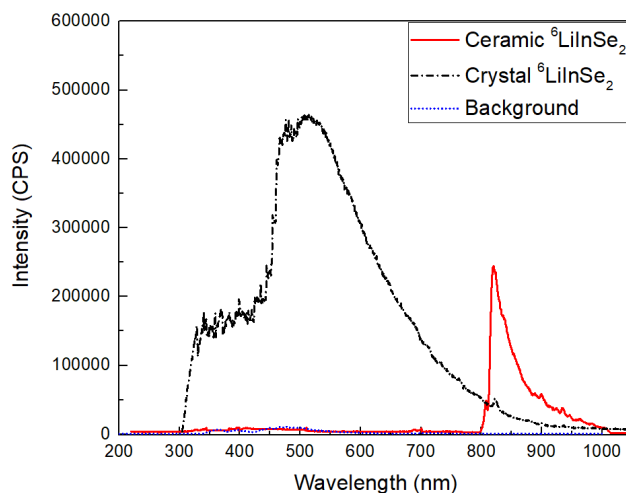

Figure 4.3: Emission spectra of the ^{6}LiInSe$_2$ crystal and ceramic show a shift to the infrared for the ceramic while the crystal emits in the visible.

4.3.4   Chemical Composition

Scanning electron microscopy with energy dispersive X-ray spectroscopy (SEM/EDS) was performed on the sample to determine the chemical composition of the ceramic sample. This data is shown in table 4.1.and figure 4.4

Indium and selenium reasonably reflect their initial stoichiometric ratios. Lithium concentration could not be measured via EDS but is considered to be uniform across the measured region of the sample. There is a moderate amount of oxygen in the sample which is believed to be a contributor to the lower energy absorption edge. The silicon seen in the table are spectral artifacts from the internal fluorescence generated by the interaction between X-rays and the silicon detector in the instrument.
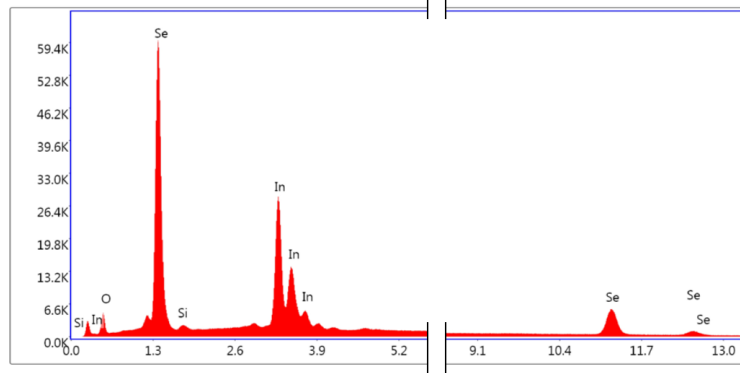
Figure 4.4: EDS data of the ceramic sample shows well defined selenium and indium peaks. Potential contamination from oxygen can be seen at lower levels.

EDS Measurements			
Element	Weight %	Atomic %	Error %
Oxygen	3.42	16.17	8.88
Silicon	0.29	0.78	11.57
Indium	30.61	20.16	1.52
Selenium	65.68	62.89	3.14

Table 4.1: EDS measurements showing weight and atomic percentages as well as margin of error.
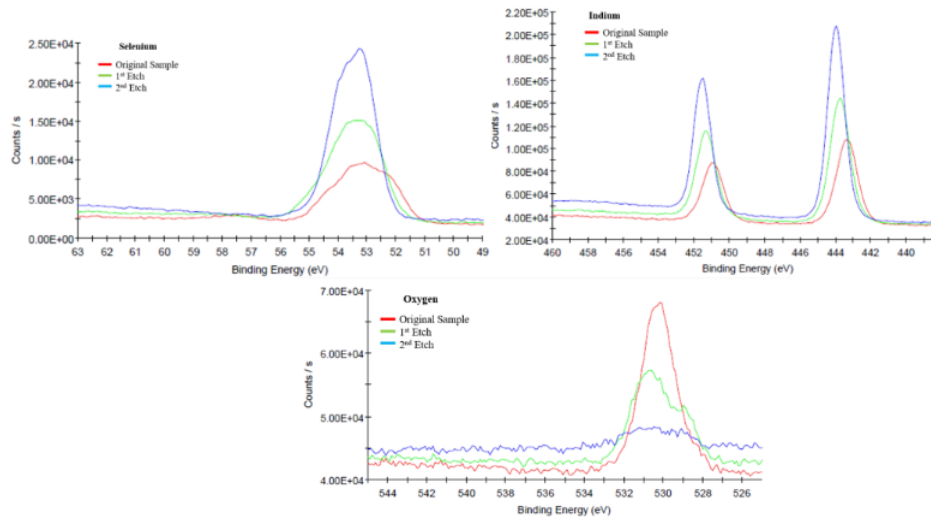

Figure 4.5: Data from XPS measurements show decreasing oxygen peaks and increasing indium and selenium peaks after each ablation.

Further elemental measurements were conducted with an XPS micro-probe to discover the depth at which oxygen abundance disappears. This is seen in figure 4.5. A monatomic

argon ion beam of 1.0 keV ablated microns from the surface if samples for 380 s. Using an Al k-alpha x-ray source with 1.4 keV energy elemental maps were taken at each level. Lithium and selenium have overlapping peaks making it difficult to distinguish between the two elements. Regardless, after each ablation, there is an increase in indium, and potentially both lithium and selenium. Most importantly, oxygen levels decrease at each level.

4.3.5 Scintillation Properties

Alpha radiation results from a 0.9 μCi ^{241}Am source can be seen in figure 4. This data was obtained by directly irradiating the sample from its top face so that there was no direct alpha radiation on the PMT window. The light produced from the alpha particles display a prominent peak at 2.42 eV in the crystal and a 2.65 eV peak in the ceramic.
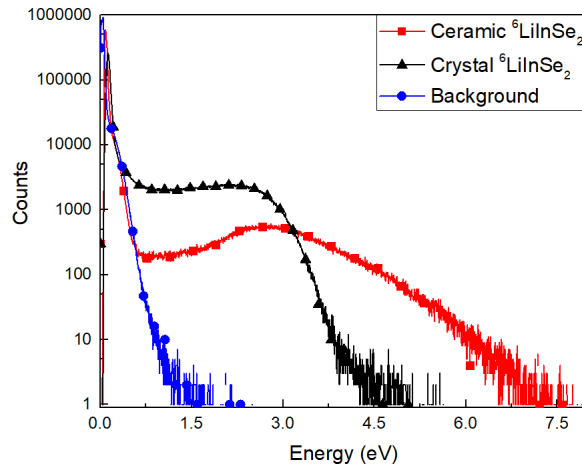
Figure 4.6: Alpha response from an ^{241}Am source of crystal and ceramic ^{6}LiInSe$_2$ in counts integrated over 300 seconds using a photomultiplier tube.

In the region of interest, the ceramic has a lower count rate than the crystal. This is due to the inherent scattering in a polycrystalline material as well as the lower absorption edge. These absorbed photons never reach the photodetector which lead to a decrease in count rate. Even though the count rate is lower and the peak is shifted, the presence of a peak in this ceramic is an indicator that even starting with large particle sizes, a radiation response is possible .
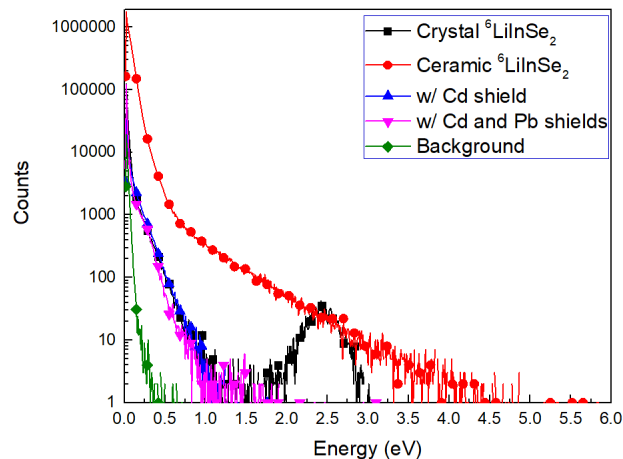
Figure 4.7: Neutron response from ^{252}Cf of crystal and ceramic ^{6}LiInSe$_2$ in counts integrated over 1200 seconds. Neutrons were moderated with paraffin blocks to obtain the thermal neutron spectra.

Thermal neutron radiation results from an 81.6 μCi ^{252}Cf source with a flux of 3.5 x 10^5 n/s can be seen in figure 5. Although the incorporation of ^6Li is the primary element for thermal neutron capture, the cross section of ^{115}In cannot be ignored as its production of low energy gamma rays decrease the neutron detection efficiency by at most 18% [38]. With the use of 5.08 cm Pb filter, and a 0.25 cm Cd filter, thermal neutrons and gamma rays are distinguishable. Both ceramic and crystal ^{6}LiInSe$_2$ show a neutron response. The crystal displays a peak at 2.44 eV while the ceramic spectrum show a continuum. This continuum in the ceramic is attributed to diffuse scattering. Even though a peak is not present in the neutron spectrum, this response indicates ^6Li is still present and has not escaped the ceramic sample during hot pressing and sintering.

Although the ceramic displays a continuum, there is a definite neutron response from the ceramic sample. Unexpectedly, the results show that there is a greater neutron response in the ceramic even though its crystal counterpart has a larger surface area. This increase can be caused by light scattering on grains and boundaries only from the surface layer close to the photodetector. This essentially makes the ceramic a very thin scintillator. Traditionally, the thickness of a scintillator effects its light output. Thinner samples should have a

higher light yield when exposed to low energy particles. The ceramic has a higher light yield than the crystal due to the scattering of light and only a surface irradiation.
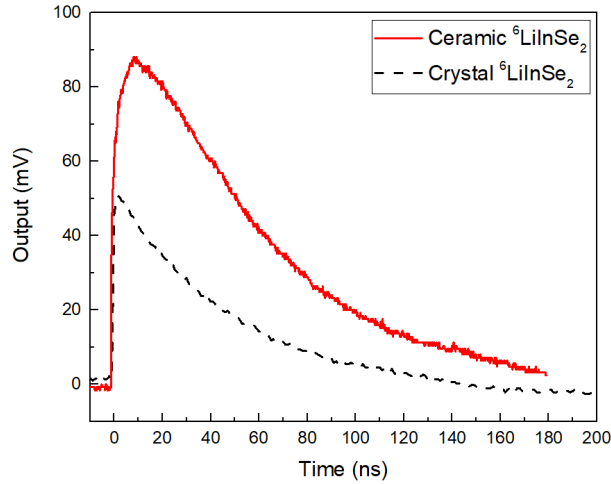

Figure 4.8: Decay timing after irradiation with ^{241}Am alpha source with a Hamamatsu R6231-100 PMT. Decay constants were determined to be 70.8 ± 1.4 ns for ceramic and 51.3 ± 13 ns for the crystal.

Pulse decay profiles of crystal and ceramic ^{6}LiInSe$_2$ were generated using an alpha source. The measurement of decay constants were 70.8 ± 1.4 ns for the ceramic and 51.3 ± 13 ns for the crystal and are shown in figure 6. The ceramic decay time lies between the reported fast and slow decay times of [26]. A fast decay time is necessary so that fast signal pulses can be generated. If light emission of one pulse occurs within the decay of a previous pulse, a summed peak can potentially be produced [39]. This leads to an inaccurate representation of the scintillator's brightness. The fast decay time of 70.8 ± 1.4 ns is an indicator that this ceramic can be used in a practical setting.

4.4   Conclusion

Ceramic and crystal ^{6}LiInSe$_2$ scintillators were prepared via uniaxial hot pressing and vertical Bridgman growth, respectively. The information provided in this paper serve as the first ceramic ^{6}LiInSe$_2$ alpha and neutron radiation detectors. Absorption edge and emission have been experimentally investigated with an absorption edge at 1.86 eV (667 nm) and

emission at 1.51 eV (823 nm). The abrupt end of the transmissive window at wavelengths shorter than 500 nm is attributed to the yellow color of the crystal. This is similar to the sudden drop in luminescence intensity to a sloping plateau before reaching the UV cutoff. In the ceramic, there is no measurable transmission through most of the UV-Vis range. This assures that any of the observed light originates from surface scatter. However, at wavelengths above 650 nm, there is a measurable transmission window of about 2% which allows the weak emissive feature in the near-IR.

Scintillation properties were investigated where ceramic ^{6}LiInSe$_2$ detects both alpha and neutron radiation. For neutron detection, ceramic ^{6}LiInSe$_2$ material does not currently possess the resolution that its crystal counterpart has, but thermal neutron radiation response is clearly visible in the ceramic sample. The continuum, which is due to diffuse inelastic scattering, would probably be present in any ceramic of this quality. Currently, the neutron response does not resolve a peak which is required to distinguish neutrons and gammas in a high gamma flux areas. ^{6}LiInSe$_2$ is a lower Z material and thin so the intrinsic gamma absorption efficiency is low. This makes the need for electronic differentiation on the neutron signal less necessary.

The ceramic sample displays a prominent peak at 2.65 eV under alpha irradiation. Although slightly shifted from its crystal counterpart, these results show that a ceramic ^{6}LiInSe$_2$ radiation detector is possible. The ceramic sample can be prepared quickly due to the incorporation of ^{6}Li in its structure. Also, the ceramic sample can be operated at room temperature, and a has a decay time that can compete with a single crystal ^{6}LiInSe$_2$. However, optimization is necessary. The ceramic material's low transparency and high scattering needs to be improved upon. This energy shift in the alpha radiation spectrum also needs to be further investigated. Further annealing treatment is expected to enhance the optical properties of ^{6}LiInSe$_2$ based on current literature [40] [41].

CHAPTER 5

Methodological Reflections

5.1 Grain Size

This work has information about the theory of grain growth and the propagation of growth faces and their importance in polycrstalline materials yet there is no direct information or data about ^{6}LiInSe$_2$ in its ceramic form. This section will include the various methods attempted to find the average grain size and why they were not successful.

5.1.1 Optical Microscopy

Grain size approximation was first attempted using a Nikon LV100N POL polarizing light microscope. This microscope uses a 12V 50W halogen light bulb allowing the samples to be back-lit. Initial images showed a rough non-uniform surface with no evidence of grain size. Due to the fragile nature of some samples, hand polishing caused them to fracture and break. To remedy this and to remove any surface contaminants, samples were chemically polished for 30 seconds using a methanol-bromine solution. A representative image of before and after polishing can be seen below.
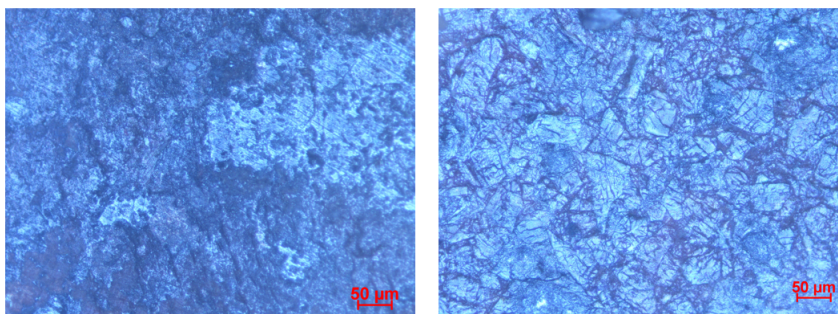

Figure 5.1: ^{6}LiInSe$_2$ ceramic before chemical polishing (left) and after chemical polishing (right).

Chemical polishing came with its own host of problems as some of the samples disintegrated in the solution. The surviving samples resulted in images similar to figure 5.1 above.

Images from the optical microscope show a cracked surface that is not representative of actual grain size. Furthermore, this device is capable of viewing internal layers of materials. This was not possible for the samples in this study most likely due to the multiple internal scattering inherent in polycrystalline materials.

5.1.2 Scanning Electron Microscopy

Scanning electron microscopy (SEM) was used to obtain a higher magnification image. Samples were polished for 30 seconds in a bromine-methanol solution and dried before measurements. There is a 1000X magnification with a working distance of 10.2mm. SEM images can be seen below in image 5.2.

Figure 5.2: Polished ^{6}LiInSe$_2$ ceramic under 1000X magnification with a 10.2mm working distance.

This image is similar to the optical microscope images and unfortunately, grain size was unable to be obtained. Further magnification did not show any grain size either. One issue that is common in SEM is sample charging. This happens when there is no conducting path for electrons to flow. Sample charging causes the image to drift and blur creating false images. This easily remedied by grounding the sample with conductive tape.

5.1.3 Atomic Force Microscopy

Atomic force microscopy (AFM) is a very high resolution type of scanning probe that is capable of topographical imaging. It does this with the use of a cantilever moving across the

surface with Van der Waals forces changing the amplitude. This changes the amount of light reflected into the photodiode and a resulting image is produced as seen below. Although
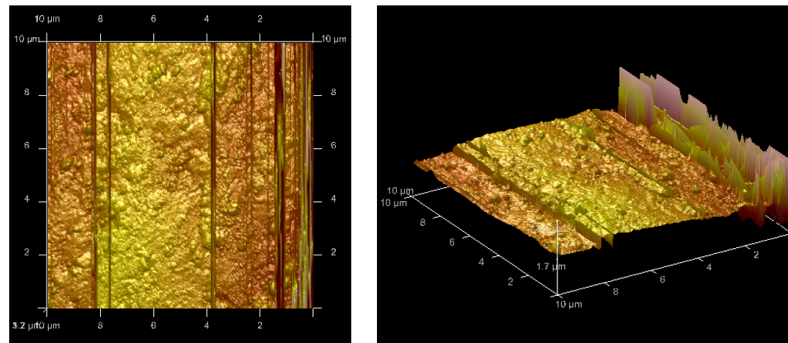

Figure 5.3: Polished ^{6}LiInSe$_2$ ceramic AFM image in 2D (left) and 3D (right).

AFM results are useful this technique did not reveal the grain size as expected. The issue deals with the sensitivity of the instrument and the quality of the samples. Sample used for an AFM study must have a higly polished surface free of contaminants. The samples in this work did not meet the requirements of the AFM polishing standard. Furthermore, the AFM tip was damaging to the ceramics as seen in figure 5.4.

Figure 5.4: Damage from Atomic for microscope cantilever tip

The images produced from the AFM study are unreliable due to the damage in ceramic samples and the inability to achieve the required polishing standard.

5.1.4 Optical Coherence Tomography

Optical coherence tomography (OCT) is a technique that uses low coherence light to create 2D and 3D images within optical scattering media. OCT is typically used on bi-

ological tissue but its ability to image scattering media made it a potential candidate for ^{6}LiInSe$_2$ ceramics. Dr. Yuankai (Kenny) Tao of the Vanderbilt Biomedical Engineering Department agreed to conducted these measurements. A typical OCT can be seen below in figure 5.5 below.
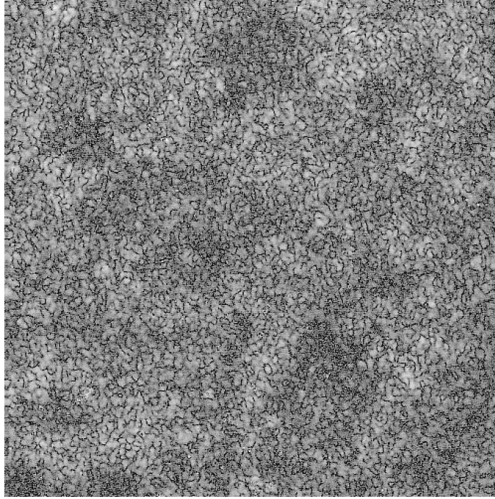
Figure 5.5: Optical coherence tomography image of ^{6}LiInSe$_2$ ceramic. The image is 1mm X 1mm

This data has been deemed inconclusive. It is not clear what the darker patches represent or why there was no change in what is believed to be grain size after annealing. There may be useful information in those data. Due to the global pandemic at the time of the experiments, it was impossible to work closely with Dr. Tao. It is recommended to work closely with Dr. Tao or any other OCT expert if this avenue is to be explored further.

5.2 Sample Preparation

Many of the issues that lead to the inability to find grain size come from sample preparation. Experimentation contains much trial and error based on the current literature. This section contains some of the pitfalls that finally led to a usable sample.

5.2.1 Oxidation

The samples in this study all come from a well documented crushed ^{6}LiInSe$_2$ crystal. When in an inert environment such as a glovebox, there is no change in color of the powder which is to be expected. Upon removal from the inert environment, the powder quickly oxidizes and turns orange-brown. This can be avoided by pressing and heating within the glovebox or using a vacuum chamber that allows both heat and pressing. After heating and pressing, the sample will still oxidize and turn orange-brown if not in an inert environment. If radiation measurements are to be conducted on a pristine sample, the ceramic must be encapsulated or the radiation setup must be moved to an inert atmosphere.

Regardless of how old the sample is or how it was initially heated and pressed, it is possible to remove this oxidation through annealing. Currently, annealing is a required step to achieve optimal radiation response. Assuming standard temperature, the thicker the sample, the longer the anneal time. It is highly recommended to use a transparent furnace when annealing to see the gradual change back to stoichiometric color. This will eliminate the need to open the furnace or remove the sample from the furnace.

5.2.2 Sample Durability

Currently, sample durability is most controllable during sample preparation before annealing. The main issue with the current setup used in this work is the inability to get equal pressure on the powder resulting in a non-uniform sample. The best solution for this issue is isostatic pressing. This technique allows for equal pressure and heat throughout the powder. A simpler solution is to use a hemisphere on top of the powder. A hemisphere will theoretically distribute the pressure equally.

To further improve sample uniformity and durability, having an exact control of the heating temperature is key. Be sure to get a temperature profile of the die used. During pressing, heating and cooling should have a slow ramp rate. A slow heat rate enables equal heating of the powder preventing fragile edges.

5.3 Future Work

If this work is to be continued it would be worth attempting to start from the synthesis step of Bridgman crystal growth rather than growing an entire boule. Before growth, the material is still ^{6}LiInSe$_2$ just not in a single crystalline form. This will save an inordinate amount of time and limit lithium diffusion which decreases the amount of excess lithium needed for ^{6}LiInSe$_2$ crystals. If starting from a crystal, it is best to crush the crystal as needed to slow down any oxidation that is likely to occur.

Many techniques used in this work was an attempt to achieve transparency. Unfortunately, ^{6}LiInSe$_2$ does not have an optically isotropic structure, and so full transparency is essentially out of reach. Nevertheless, a high degree of translucency can still be achieved if the grains are kept small enough, their size distribution narrow enough, and pores few enough to keep scattering at a minimum. A focus on understanding how grain size and orientation may have changed during the annealing process will elucidate peak formation in alpha radiation response.

Neutron response should also be further explored. Current results do not resolve a peak and there is an abundance of what seems to be neutron counts. Due to the distance between the annealing chamber and neutron source, immediate response was not possible. A systematic study between increased oxidation and neutron radiation response should be held.

References

[1] Akio Ikesue and Yan Lin Aung. Ceramic laser materials. *Nature photonics*, 2:721–727, 2008.

[2] Glenn F Knoll. *Radiation detection and measurement*. John Wiley Sons, 2010.

[3] US.NRC. Alpha particle. *United States Nuclear Regulatory Commission*, 2016.

[4] Arecchi Angelo V, Messadi Tahar, and Koshel R John. Field guide to illumination. *SPIE Press*, 2007.

[5] Lucio Cerrito. Radiation and detectors. *Cambridge University*, 2017.

[6] JC Inkson and Dirk Ter Haar. Many-body theory of solids: An introduction. *Physics Today*, 38(5):85, 1985.

[7] Syed Naeem Ahmed. *Physics and engineering of radiation detection*. Academic Press, 2007.

[8] Govindhan Dhanaraj, Kullaiah Byrappa, Vishwanath Prasad, and Michael Dudley. *Springer handbook of crystal growth*. Springer Science & Business Media, 2010.

[9] Ling Zang. *Energy efficiency and renewable energy through nanotechnology*. Springer, 2011.

[10] Alekse Vasilevich Shubnikov et al. *Growth of Crystals: Volume 2*, volume 2. Springer Science Business Media, 2012.

[11] PW Bridgman. Certain physical properties of single crystals of tungsten, antimony, bismuth, tellurium, cadmium, zinc, and tin. In *Proceedings of the American academy of arts and sciences*, volume 60, pages 305–383. JSTOR, 1925.

[12] Mark Fox. Optical properties of solids, 2002.

[13] Cornelis Klein, Barbara Dutrow, and James Dwight Dana. *The 23rd edition of the manual of mineral science:(after James D. Dana)*. Number 549 KLE. 2007.

[14] Richard T Kouzes, James H Ely, Luke E Erikson, Warnick J Kernan, Azaree T Lintereur, Edward R Siciliano, Daniel L Stephens, David C Stromswold, Renee M Van Ginhoven, and Mitchell L Woodring. Neutron detection alternatives to ^{3}He for national security applications. *Nuclear Instruments and Methods in Physics Research Section A: Accelerators, Spectrometers, Detectors and Associated Equipment*, 623(3):1035–1045, 2010.

[15] T Nakamura, A Ohzu, K Toh, K Sakasai, H Suzuki, K Honda, A Birumachi, M Ebine, H Yamagishi, M Takase, et al. Neutron-sensitive $ZnS/^{10}B_2O_3$ ceramic scintillator detector as an alternative to a ^{3}He-gas-based detector for a plutonium canister assay

system. *Nuclear Instruments and Methods in Physics Research Section A: Accelerators, Spectrometers, Detectors and Associated Equipment*, 763:340–346, 2014.

[16] Anthony J Peurrung. Recent developments in neutron detection. *Nuclear Instruments and Methods in Physics Research Section A: Accelerators, Spectrometers, Detectors and Associated Equipment*, 443(2-3):400–415, 2000.

[17] Keenan J Wilson, Roumani Alabd, Mehran Abolhasan, Mitra Safavi-Naeini, and Daniel R Franklin. Optimisation of monolithic nanocomposite and transparent ceramic scintillation detectors for positron emission tomography. *Scientific Reports*, 10(1):1–15, 2020.

[18] Yutaka Fujimoto, Takayuki Yanagida, Hideki Yagi, Takagimi Yanagidani, and Valery Chani. Comparative study of intrinsic luminescence in undoped transparent ceramic and single crystal garnet scintillators. *Optical Materials*, 36(12):1926–1929, 2014.

[19] Takayuki Yanagida, Kei Kamada, Yutaka Fujimoto, Hideki Yagi, and Takagimi Yanagitani. Comparative study of ceramic and single crystal Ce: GAGG scintillator. *Optical Materials*, 35(12):2480–2485, 2013.

[20] Yukio Ito, Hiromichi Yamada, Minoru Yoshida, Hideji Fujii, Gyozo Toda, Hiroshi Takeuchi, and Yasuo Tsukuda. Hot isostatic pressed Gd_2O_2S: Pr, Ce, F translucent scintillator ceramics for x-ray computed tomography detectors. *Japanese journal of applied physics*, 27(8A):L1371, 1988.

[21] Daniel S Hamm, Mikah Rust, Elan H Herrera, Liviu Matei, Vladimir Buliga, Michael Groza, Arnold Burger, Ashley Stowe, Jeff Preston, and Eric D Lukosi. Semiconducting lithium indium diselenide: Charge-carrier properties and the impacts of high flux thermal neutron irradiation. *Applied Physics Letters*, 112(24):242104, 2018.

[22] Yousif K Kharaka and JS Hanor. Deep fluids in the continents: I. sedimentary basins. *Treatise on Geochemistry*, 5:605, 2003.

[23] Varley F Sears. Neutron scattering lengths and cross sections. *Neutron news*, 3:26–37, 1992.

[24] HJ Beister, S Ves, W Hönle, K Syassen, and G Kühn. Structural phase transitions and optical absorption of liinse 2 under pressure. *Physical Review B*, 43:9635, 1991.

[25] Yanlu Li, Weiliu Fan, Honggang Sun, Xiufeng Cheng, Pan Li, and Xian Zhao. Computational insight into the effect of monovalent cations on the electronic, optical, and lattice dynamic properties of $XInSe_2$ (X= Cu, Ag, Li). *Journal of Applied Physics*, 109:113535, 2011.

[26] Brenden Wiggins, Michael Groza, Eugene Tupitsyn, Eric Lukosi, Keivan Stassun, Arnold Burger, and Ashley Stowe. Scintillation properties of semiconducting $^6LiInSe_2$ crystals to ionizing radiation. *Nuclear Instruments and Methods in Physics Research Section A: Accelerators, Spectrometers, Detectors and Associated Equipment*, 801:73–77, 2015.

[27] TT Basiev, ME Doroshenko, VA Konyushkin, VV Osiko, PP Fedorov, VA Demi-denko, KV Dukel'skii, IA Mironov, and AN Smirnov. Fluoride optical nanoceramics. *Russian Chemical Bulletin*, 57:877–886, 2008.

[28] Ricardo Castro and Klaus Van Benthem. *Sintering: mechanisms of convention nanodensification and field assisted processes*, volume 35. Springer Science & Business Media, 2012.

[29] JE Burke. Some factors affecting the rate of grain growth in metals. *Aime Trans*, 180:73–91, 1949.

[30] Andreas Michels, CE Krill, H Ehrhardt, R Birringer, and DT Wu. Modelling the influence of grain-size-dependent solute drag on the kinetics of grain growth in nanocrystalline materials. *Acta materialia*, 47(7):2143–2152, 1999.

[31] E Rabkin. On the grain size dependent solute and particle drag. *Scripta materialia*, 42(12):1199–1206, 2000.

[32] E Carnall, S.E. Hatch, and W.F. Parsons. Optical studies on hot-pressed polycrystalline CaF_2 with clean grain boundaries. *The Role of Grain Boundaries and Surfaces in Ceramics*, pages 165–173, 1966.

[33] Yao Zhu, Sen Qian, Zhigang Wang, Hao Guo, Lishuang Ma, Zhile Wang, and Qi Wu. Scintillation properties of GAGG: Ce ceramic and single crystal. *Optical Materials*, 105:109964, 2020.

[34] MA Illarramendi, I Aramburu, J Fern*á*ndez, R Balda, SN Williams, JA Adegoke, and MA Noginov. Characterization of light scattering in translucent ceramics. *Journal of the Optical Society of America B*, 24(1):43–48, 2007.

[35] E Tupitsyn, P Bhattacharya, E Rowe, L Matei, M Groza, B Wiggins, A Burger, and A Stowe. Single crystal of $LiInSe_2$ semiconductor for neutron detector. *Applied Physics Letters*, 101(20):202101, 2012.

[36] M Magesh, A Arunkumar, P Vijayakumar, G Anandha Babu, and P Ramasamy. Investigation of optical property in $LiInSe_2$ single crystal grown by bridgman stockbarger method using stepper translations for mid ir laser application. *Optics & Laser Technology*, 56:177–181, 2014.

[37] C ASTM. Standard test methods for apparent porosity, water absorption, apparent specific gravity, and bulk density of burned refractory brick and shapes by boiling water. ASTM, 2010.

[38] Jean Blachot. Nucl. data sheets 113. *ENSDF*, 2391, 2012.

[39] Amretashis Sengupta. Basic solid-state physics and crystallography. *Introduction to Nano.*, pages 27–57, 2015.

[40] Chansun Park, Muhammad Nasir Ullah, Chanho Kim, Shinhaeng Cho, and Jung-Yeol Yeom. Investigation of optical properties of ceramic Ce: GAGG by high temperature annealing. *Journal of the Korean Physical Society*, 75(12):962–967, 2019.

[41] Shuilin Chen, Benxue Jiang, Qiangqiang Zhu, Wanqiu Ma, Ge Zhang, Yiguang Jiang, Weerapong Chewpraditkul, and Long Zhang. Effect of annealing atmosphere on scintillation properties of GYGAG: Ce, Mg scintillator ceramics. *Nuclear Instruments and Methods in Physics Research Section A: Accelerators, Spectrometers, Detectors and Associated Equipment*, 942:162360, 2019.